The Astrophysical Journal, 607:540–553, 2004 May 20

A COMPARISON OF CME-ASSOCIATED ATMOSPHERIC WAVES OBSERVED IN CORONAL (Fe XII 195 Å) AND CHROMOSPHERIC (He I 10830 Å) LINES

Holly R. Gilbert,[1] Thomas E. Holzer,[1] Barbara J. Thompson,[2] and Joan T. Burkepile[1]

Received 2003 July 7; accepted 2004 January 29

ABSTRACT

Although "Moreton" waves have historically been observed in Hα data, more recently waves have also been observed in chromospheric He I λ10830 images obtained at the Mauna Loa Solar Observatory. In an effort to better understand the nature of chromospheric waves and their relationship to coronal waves observed in EUV Imaging Telescope (EIT) data, we focus on two events in which waves are observed simultaneously in He I λ10830 and Fe XII λ195, lines that are formed in the chromosphere and the corona, respectively. Comparing the waves observed in these two lines allows the determination of the spatial relationship between coronal and chromospheric waves and thus aids in the understanding of the underlying physics of waves in the solar atmosphere. The main goal of this work is to begin an investigation into whether both coronal and chromospheric waves are mechanical (e.g., MHD waves) by looking at their spatial relationship. We find that the chromospheric waves in these two events are cospatial with their coronal counterparts, indicating that they are not mechanical in nature but are chromospheric imprints of mechanical waves propagating through the corona. This conclusion is based on the nature of the formation of the He I absorption line.

Subject headings: MHD — Sun: chromosphere — Sun: corona — waves

1. INTRODUCTION

1.1. *Moreton Waves*

Moreton waves (Moreton 1961; Smith & Harvey 1971) were first observed in Hα using off-band observations, which allow better detection of faint moving disturbances than do on-band observations. Some of the earliest observations of these waves show disturbances propagating over great distances across the solar disk as darker "clouds" relative to the background (Athay & Moreton 1961). They are also observed as lighter clouds relative to the background intensity, the difference in appearance resulting from use of off-band observations (depending on which wing the observations are made, dark or light "clouds" are possible). Another signature of a wave in Hα observations is a diffuse brightening of the chromosphere when using on-band observations, which may be representative of a wave front. Motivation to search for these moving disturbances originated from observations of two interesting, apparently related phenomena: impulsive phases in flares, in which the edges of flares undergo a rapid (but short-lived) expansion, and filaments becoming disturbed. It was the search for a possible connection between these two types of observations that led to the discovery of traveling waves.

The "explosive phase" seen in some flares is a sudden increase in brightness on a timescale that is short compared with the total time of rise to maximum brightness. Sudden increases in brightness are associated with a rapid expansion of the flare border at a velocity of about 400 km s^{-1} (Athay & Moreton 1961). Some flares demonstrating this explosive phase also eject faint clouds as described above, but the faint clouds usually become invisible shortly after leaving the flare. Evidence of the continuation of the traveling disturbances from flare sites is manifested in observations (Athay & Moreton 1961) of abruptly disappearing or activated filaments. Distant filaments (600,000 to 700,000 km from the flare site) sometimes undergo a temporary fading or disappearance, reappearing after only a minute or, in some cases, after much longer periods; these are referred to as "winking" filaments. The disappearance of a filament, however, is not the only type of filament disturbance that can indicate the passage of a wave; some filaments respond by oscillating back and forth without disappearing as the wave propagates through. Early measurements of the average speed for wavelike disturbances involved taking the distance from the flare where the wave is assumed to have originated to the disturbed filament (either winking or oscillating) and dividing it by the time interval between the explosive phase of the flare and the filament activation (Moreton 1960). Inferred velocities measured in this manner seemed to be consistent with the first direct measurements (off-band) of waves observed in Hα.

One property of the earliest observed Moreton waves is that their range of speed is approximately 550 to 2500 km s^{-1} (Smith & Harvey 1971), with an average speed of about 1000 km s^{-1} (Moreton 1960; Athay & Moreton 1961; Smith & Harvey 1971). Moreton waves are generally more easily detectable near the flare site where they originate, but one of the early detectable moving disturbances (described as a cloud) was observed as far as 200,000 km from the flare site (Athay & Moreton 1961). Early observers of Hα waves assumed that flares directly initiate wavelike disturbances (Moreton 1961; Athay & Moreton 1961; Uchida 1968; Smith & Harvey 1971), and although this may hold true, there has been some speculation more recently as to whether waves can be generated by coronal mass ejections (CMEs), which were first detected in the 1970s with the launch of the *Orbiting Solar Observatory* (Tousey 1973). The question regarding the initiation processes of waves has been revisited since the discovery of waves propagating in the corona (Thompson et al. 1998, 1999) observed by the Extreme Ultraviolet Imaging Telescope (EIT) aboard the *Solar and Heliospheric Observatory* (*SOHO*).

[1] High Altitude Observatory, National Center for Atmospheric Research, Boulder, CO 80307-3000; iggy@ucar.edu, holzer@ucar.edu, iguana@ucar.edu.
[2] NASA Goddard Space Flight Center, Code 682, Greenbelt, MD 20771.

1.2. *Coronal (EIT) Waves*

Coronal waves have been systematically observed with the EIT telescope (launched in 1995 December), and are thus commonly labeled "EIT waves," although Neupert (1989) presented evidence of wavelike phenomena in coronal emission lines. Coronal waves have also been observed by the *TRACE* (*Transition Region and Coronal Explorer*) satellite (Wills-Davey & Thompson 1999). EIT waves are globally propagating coronal disturbances seen in extreme ultraviolet (EUV) radiation, which emanate from a central radiant point (inferred in some cases, while directly observed in others) and travel across the visible solar surface. Several hundred EIT waves have been catalogued since EIT began observing, but whether these are coronal counterparts to Moreton waves (we use the term Moreton waves in conjunction with Hα observations only for the remainder of the present paper) has been an intriguing question since their discovery. In some recent studies Moreton waves have been found to be cospatial with EIT waves (Khan & Aurass 2002; Warmuth et al. 2001; Pohjolainen et al. 2001; Thompson et al. 2000b). Eto et al. (2002) recently found that a Moreton wave and an EIT wave produced by a flare event are not cospatial and have very different velocities. If a relationship exists between EIT waves and Moreton waves, the nature of such a relationship is not well understood. The general description of EIT waves is consistent with that of Moreton waves, but properties such as average speed and distance traveled are notably different. EIT waves usually have a leading front observed in emission traveling between 200 and 600 km s^{-1} (Thompson et al. 1999) that sometimes can be followed across the entire solar disk. The distance to which EIT waves can be followed is usually much larger than that for Moreton waves. Although EIT waves appear to travel slower on average than Moreton waves, the apparent discrepancy may be related to the difference in temporal cadence between the EIT data and the Hα data. EIT has a temporal cadence of $\sim$10–30 minutes, which limits the ability to observe waves traveling at the higher end of the velocity range of Moreton waves. Second, mean velocities are usually considered to characterize Moreton and EIT wave propagation, without taking into account deceleration, which could be significant if the EIT wave begins as a relatively strong shock wave or if the waves moves from a region of higher characteristic speed (viz., fast-mode speed) to one of lower characteristic speed. This may result in higher apparent velocities for Moreton waves, since they generally can only be followed a short distance from their origin, whereas EIT waves can sometimes be tracked across a majority of the solar disk (Warmuth et al. 2001). A third reason for the discrepancy in the range of speeds may arise from potentially different driving mechanisms, which we discuss in the section on theories about drivers of waves (§ 1.4). Another very interesting and common characteristic of EIT wave propagation is its modification by the presence of magnetic solar features such as active regions and neutral lines (Thompson et al. 1999). One last property of EIT waves worth noting is their association with other solar phenomena. EIT waves show a strong association with flares, but are even more strongly correlated with CMEs (Biesecker et al. 2002), and are also associated with other solar phenomena such as type II radio bursts and dimmings (defined in § 4.2). Moreton waves are also strongly correlated with solar flares (Moreton 1961; Athay & Moreton 1961; Uchida 1968; Smith & Harvey 1971), but there is no comprehensive study of associations with phenomena other than flares.

1.3. He I *Waves (Chromospheric Waves)*

More recently wavelike phenomena have been observed in He I λ10830 data (hereafter referred to as He I) taken at the Mauna Loa Solar Observatory (MLSO). Waves observed in the He I data usually have a leading wave front traversing the visible solar disk that appears dark because of enhanced absorption of the background photospheric continuum. The first He I wave was observed in 1997, but we began looking for He I waves systematically starting in 1999 June, and since then approximately 12 "good" waves (defined as those showing a clear propagating disturbance that is distinguishable from other phenomena such as erupting filaments) have been observed in the He I data (two other definite waves were observed in 1998). Since 1999 June about 31 other events classified as "possible waves" were observed in He I. The range of speeds for waves observed in He I is very similar to that of EIT waves (i.e., $\sim$200–600 km s^{-1}), and like EIT waves, the He I wave propagation is modified by the presence of magnetic features such as active regions. All of the He I events labeled "good" have a flare association and generally appear to originate from a fairly localized region at the flare site. In at least one instance, a leading wave front is observed preceding other visible waves originating from the same general flare region. A previous study was conducted by Vršnak et al. (2002) in which the kinematics of He I waves are compared with those of waves observed in Hα and Fe XII. Some of the details of their interpretation are presented in § 4.2.

1.4. *Drivers of Waves*

The discovery of EIT waves has led to a debate on what is driving such waves. Moreton (1960) suggests that flares trigger the wavelike disturbances observed in Hα and, in particular, those flares that show a distinct "explosive" development in which the intensity increases sharply and the luminous borders expand outward at several hundred km s^{-1} following the initial brightening. Early observers of Moreton waves generally accepted that flares caused waves, but the discovery of CMEs and EIT waves led to another theory regarding driving mechanisms. There are two main theories on the drivers of waves: flare-driven and CME-driven. The "flare-driven" theory (sometimes referred to as the "blast-wave" theory) proposes that a flare produces an initial pressure pulse that propagates through the corona as a fast-mode MHD shock (Steinolfson et al. 1978; Vršnak & Lulić 2000). In this theory Moreton waves observed in Hα represent the chromospheric ground tracks of the three-dimensional dome-shaped coronal shock front (Uchida, Altschuler, & Newkirk 1973). Alternatively, the "CME-driven" theory (sometimes called the "piston-driven" theory) suggests CMEs act as pistons, responsible for the initiation of waves (see Cliver, Webb, & Howard 1999, and references therein). If the expulsion of a CME initiates a wave, the origin of the wave would not be a localized point source, since CMEs have finite width at their footpoints. Looking at the origin of waves is the only observational approach to differentiating between the two theories presented above, because although the initiation process differs, the waves in both scenarios quickly become freely propagating at (essentially) the local wave speed. We would like to emphasize that in both theories a pressure pulse of

finite temporal width is generated (by either a flare or a CME) and propagates through the corona. (It is worth noting that there is no observational evidence that waves at the base of the corona have steepened into shocks.) As mentioned in § 1.2, a discrepancy in the range of speeds when coronal waves are compared with Moreton waves may exist if we consider the possibility that one event can produce both CME-initiated waves and flare-driven waves. If a CME and flare produce waves nearly simultaneously from approximately the same region, the CME-initiated wave front will be found farther from the flare origin than the flare-initiated wave front, because the CME-driven wave is generated at the outer boundary of the erupting magnetic arcade, while the flare-driven wave is generated in the interior of the arcade. This is an expectation based on the picture of an erupting arcade comprising the CME and reconnection in the middle of the arcade producing a flare. In this picture, the outer erupting arcade produces a CME-driven wave by generating a pressure pulse at the boundary marking the footpoints of the arcade. In contrast, the flare-driven wave is generated where reconnection is taking place, i.e., nearer the center of the arcade than the outer boundary of the arcade footpoints. The effect mentioned above (i.e., the CME-initiated wave front will be found farther from the flare origin than the flare-initiated wave front) will be enhanced if the CME initiation precedes that of the flare. If velocity measurements are made of the CME-initiated wave (either by winking filaments or direct observation of a wave front, but in both cases assuming that the flare location and time of initiation correspond to the origin of the wave), then the measurements will yield higher velocities than corresponding measurements of the actual flare-initiated wave. If such CME-initiated wave measurements are combined with the flare-initiated wave measurements, the apparent speed will be higher than if measurements were made on the flare-initiated wave only. This potential measuring mistake could be partly responsible for the observational inference that Moreton waves have higher speeds than coronal waves, but it is also possible that the two types of waves are inherently different and thus have different ranges of velocities. As mentioned earlier, there have been recent studies that support the cospatiality of Moreton waves with EIT waves, but there are also studies that support the idea that Moreton waves are different in nature from EIT waves (Thompson et al. 2000b; Uchida et al. 2001; Eto et al. 2002).

We can conclude from earlier studies that waves observed in He I and EUV are physically related, but the detailed nature of this relationship remains unclear. Examining some of the details of this relationship is the motivation behind the present work, with the emphasis on examining waves in He I λ10830 without the assumption that these types of waves are the same as Moreton waves, which are observed in Hα. In the context of the present paper, "chromospheric waves" are those observed in He I λ10830, and we explicitly mention "Moreton waves" in the context of Hα observations only. In an effort to better understand the relationship between coronal waves (EIT waves) and chromospheric waves (He I waves), we closely study two events in which waves are observed simultaneously in both Fe XII λ195 and He I λ10830. Such a comparison allows us to determine the spatial relationship between coronal and chromospheric waves and thus aids in our attempt to understand the underlying physics of waves. We exclude Hα data in the present study because of the difficulty in measuring the diffuse front observed in on-band Hα observations taken at MLSO concurrently with the He I observations (note that the wave front is better defined and can be followed from its origin in He I data). We also feel that the inclusion of Hα data is unnecessary for achieving the main goal of this work, which is to begin an investigation into whether coronal and chromospheric waves are both mechanical waves (e.g., MHD waves) or whether chromospheric waves are simply "imprints" of mechanical waves propagating in the corona. We discuss the meaning of "imprints" in § 4 in which the formation of the He I line is explained.

The remainder of the paper is presented in the following way. The observations used in this study are presented first (§ 2) and are followed by the results obtained by measuring the spatial relationship for two events that have concurrent EIT and He I observations (§ 3). Our interpretation of these results is presented in § 4 in which a description of the formation of the He I line is followed by a discussion of a possible physical explanation of the observational results. We briefly summarize our results in § 5.

2. OBSERVATIONS

Coronal waves in this study are observed in EIT (Delaboudinière et al. 1995) full-disk Fe XII λ195 images. EIT has a spatial resolution of 2.″6 per pixel and a temporal cadence of ~10–30 minutes. The point spread function is less than or equal to 10^{-2} of the central intensity within one pixel. The Hα and He I data used were taken at the Mauna Loa Solar Observatory (MLSO) located on the island of Hawaii. MLSO operates daily (weather permitting), collecting data for about 9 hr a day (typically 17:00–02:00 UT), producing some 170 images from each of its coronal instruments. At the time of this study, MLSO was operating daily for approximately 5 hr a day (typically 17:00–22:00 UT), producing 100 images from each coronal instrument. One of the waves was observed with the Polarimeter for Inner Coronal Studies (PICS) Hα λ6563 instrument, and both waves were observed with the Chromospheric Helium Imaging Photometer (CHIP), which observes in He I λ10830. Both instruments operate with a 3 minute temporal cadence. The CHIP instrument (Elmore et al. 1998) observes in intensity and velocity (line-of-sight). The resolution of the CHIP instrument is discussed in Elmore et al. (1998): "The system spatial resolution of the CHIP instrument was inferred by computing the full width at half-maximum of the derivative of the continuum image limb profile. The full widths were measured over a range of focal positions, and the best focus was chosen. In the image field, at a position of $0.5R_0$, the width was found to be 7.″5, whereas at $1.5R_0$ the width was 9.″5. The measured pixel size subtends 2.″3." Determining CME associations in the two events studied is done using LASCO (the coronagraphs on *SOHO*) observations. The LASCO C2 and C3 coronagraphs observe the corona in total intensity from 2 to 32 R_0, with an average temporal cadence of three images hr^{-1} for C2 and two images hr^{-1} for C3.

The two wave events in this study were chosen because they are observed simultaneously in the corona and the chromosphere. The first wave we study was observed concurrently in EIT (Fe XII) and CHIP (He I) data on 2000 November 25 (Fig. 1). The active region from which this wave originates is located in the northwest quadrant and shows significant activity prior to this particular event (including a large filament eruption and associated wave the day before). There is a filament eruption beginning at ~17:13 UT (best observed in the He I velocity data) in this active region with an associated

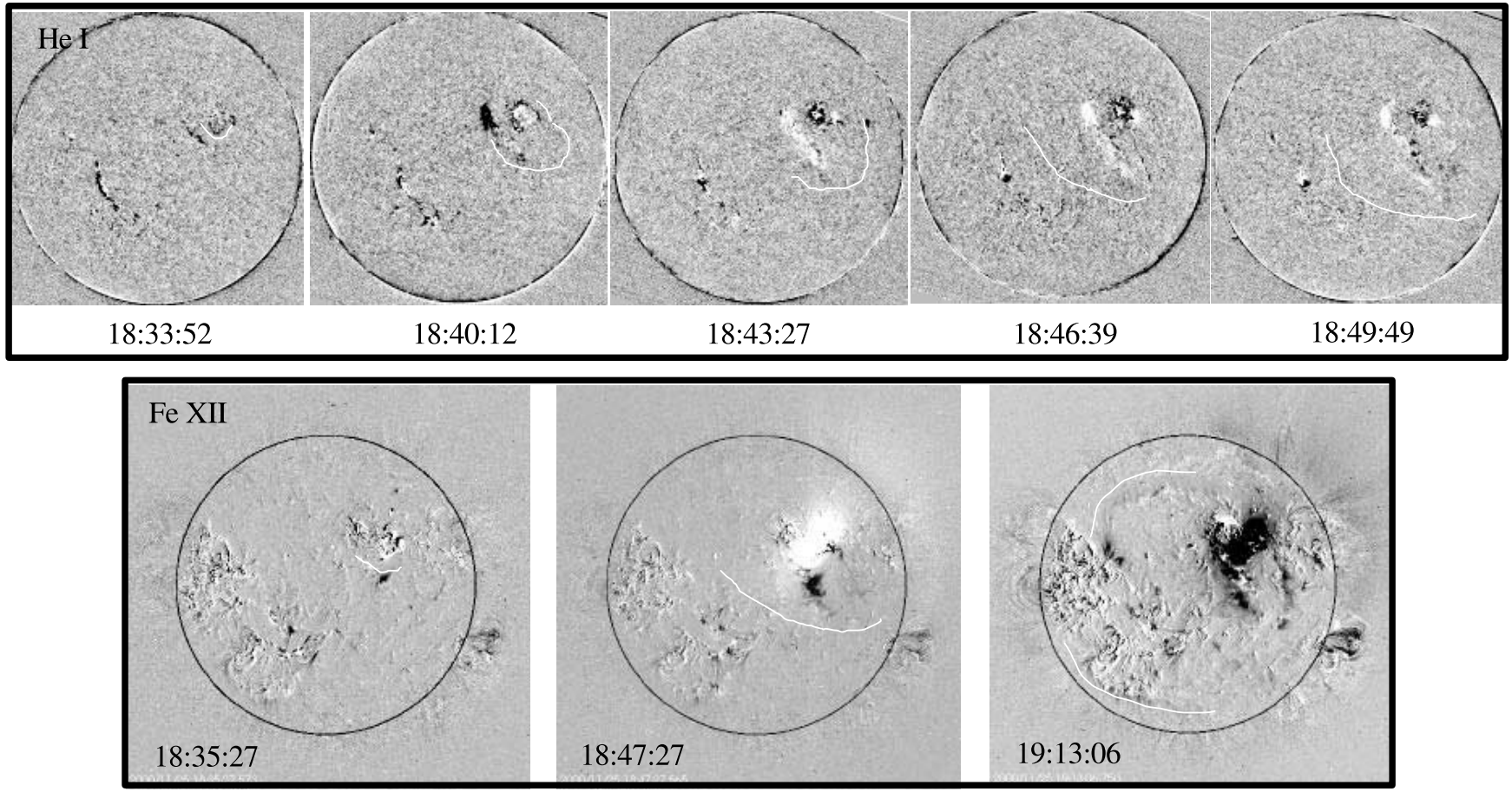

FIG. 1.—Running difference images showing the evolution of the wave event on 2000 November 25. The top panel shows the wave in five He I frames in which a line tracing out the front is added to aid in visualizing the wave evolution. The line is drawn by connecting a sequence of measurement points. The bottom panel shows the wave in three EIT Fe XII images, also with a line tracing the front to aid in visualizing the evolution.

CME at ~17:30 UT. The event under consideration occurs approximately an hour following the filament eruption, with the flare occurring in EIT at 18:35 UT (with a peak brightness visible in the 18:47 UT EIT image). The NOAA *Geostationary Operational Environmental Satellite* (*GOES-8*) satellite (which uses an X-ray monitor to identify solar flares) records a flare in the 1–8 Å bandpass coincident with the time interval of interest with a start time of 18:33 UT, a peak time of 18:44 UT, and an end time of 18:55 UT. The first He I observation of the wave occurs at ~18:24 UT, before the recorded start time of the *GOES* flare. There is another filament eruption associated with this active region occurring at 18:38 UT in the He I velocity data. The corresponding halo CME is visible in LASCO C2 at ~19:30 UT, following a brief LASCO data gap. An interesting aspect of this event is the occurrence of subsequent waves following the initial wave front originating from the same localized flare site (multiple waves are discussed in conjunction with velocity observations of waves in Gilbert & Holzer 2004). Another striking feature of the event is the appearance of He I "brightenings" (G. de Toma 2004, private communication), which correspond to EIT "dimmings," the common term used to describe transient coronal holes (see § 4.).

The second event we study was observed on 2001 January 20 in EIT, CHIP, and PICS (Hα) data in the southeast quadrant (Fig. 2 shows the evolution in EIT and CHIP). The wave is first observed in He I at ~18:37 UT, and a large LASCO C2 CME associated with this event is first visible at ~19:30 UT. Unlike the other waves observed in He I, this wave does not seem to originate from a very localized flare site but from an extended area surrounding a large two-ribbon flare. The large two-ribbon flare is first visible at 18:40 UT in the CHIP data, as well as in the Hα data obtained by the PICS instrument, and there is another smaller two-ribbon flare to the south of the larger one (also visible in CHIP and PICS), which occurs at 18:46 UT (at ~0.6R_0, P.A. 110). The *GOES* satellite records a flare start time of 18:33 UT, peak time of 18:47 UT, and end time of 18:59 UT. The smaller two-ribbon flare shows motion northward as the wave passes by the same area (traveling southward), creating some confusion in viewing the wave displacement. Although the smaller two-ribbon flare was not easily defined as such, we concluded that it was a two-ribbon flare partly based on the lack of a velocity signal in the He I velocity data (waves and related solar phenomena observed in He I velocity data are discussed in detail in Gilbert & Holzer 2004). As in the event on 2000 November 25, this event also has EIT dimmings and He I brightenings associated with it, occurring at 18:46 UT (G. de Toma 2004, private communication).

3. RESULTS

3.1. *2000 November 25*

To determine the spatial relationship between waves observed in He I data and those observed in EUV data, animations of sequential images are used to observe the propagation of the waves in He I and Fe XII. Wave evolution is most easily detected using differencing techniques. Running differences are created by subtracting each successive image from the next image, and base differences are created by subtracting the same pre-event image (called the base image) from each successive image. We use images created by differencing techniques to carefully trace the waves in the two data sets by eye. Given that these waves are extremely difficult to measure in single frames, our measuring technique involves toggling back and forth in animations to identify the wave propagation. Figure 1 shows the full disk images (created using the running difference technique) with the wave fronts traced out by eye in enough frames to show how the wave evolves in the two different data sets (the top panel is the CHIP data and the bottom is the EIT data) for the 2000 November 25 event. Figure 3 shows the wave front tracings (at all times measured) in both the Fe XII and He I data overlaid on a single grid in disk-center plane-of-sky coordinates for an easier comparison of the spatial position in the two data sets. We are able to trace the wave with confidence in six frames in the He I data (times 18:33:52–18:49:49 UT, with a 3 minute time cadence). Since EIT has a 12 minute time cadence, we are able to compare only two frames of the Fe XII wave (times 18:35:27 and 18:47:27 UT) with those measurements made in the six He I frames. To perform a detailed analysis of the spatial relationship of the He I wave front with the Fe XII wave front, we first zoom in on the waves generated close to the flare site, which corresponds to CHIP times 18:33:52 and 18:37:04 UT and an EIT time of 18:35:27 UT. Figure 4 shows a blown-up region containing these waves with scans drawn perpendicular to the direction of propagation between the two CHIP waves. Similarly, Figure 5 is a close-up of the waves traveling southward at the later times (18:46:39 and 18:49:49 UT for CHIP and 18:47:27 UT for EIT). Figure 6 also shows the waves at these later times, but the region of focus is the southeast. We use the scans in Figures 4–6 to calculate plane-of-sky velocities of the CHIP wave (in solar radii s^{-1}), as well as the velocity at the point of each scan after taking foreshortening into account (see the fifth column in Table 1). We use the following equation to correct for foreshortening:

$$d\sigma = \left[(dx)^2 + (dy)^2\right]^{1/2} \left[1 + \frac{(ax+y)^2}{(a^2+1)(1-x^2-y^2)}\right]^{1/2},$$

where $d\sigma$ is the distance along the solar surface corresponding to one of the scans, dx and dy are the x and y displacements in the plane of the sky corresponding to the scan, x and y are the disk-center plane-of-sky coordinates of the center of the scan line, and a is the plane-of-sky slope (dx/dy) of the scan line. Although the velocity varies along the wave front, the He I wave observed in CHIP on 2000 November 25 appears to be traveling on average at approximately 300 km s^{-1}.

These scans are also used to perform a detailed analysis of the cospatiality of the waves observed in He I and Fe XII. Table 1 contains such an analysis for each scan, beginning with a column representing an initial difference in measurement between the EIT front and the corresponding CHIP front, which we label Δs_0. In Table 1, Δs_0 in the seventh column after the scan numbers is the plane-of-sky distance along the scan (perpendicular to the fronts) between the CHIP front and the EIT front, and Δs in the last column is the final distance along the scan between the two fronts after correcting for the following effects. First, we must correct for wave front motion associated with the difference in observing times of the two data sets, since there is a difference of a minute or more in some of the comparison images (the plane-of-sky distance corrections to Δs_0 arising from the time differences are listed in the column labeled δs_t in the table). If our interpretation of the chromospheric "imprint" is accurate, then a correction must also be made for wave front spreading (defined in § 4.2, discussed in detail in the Appendix, and listed in the table in

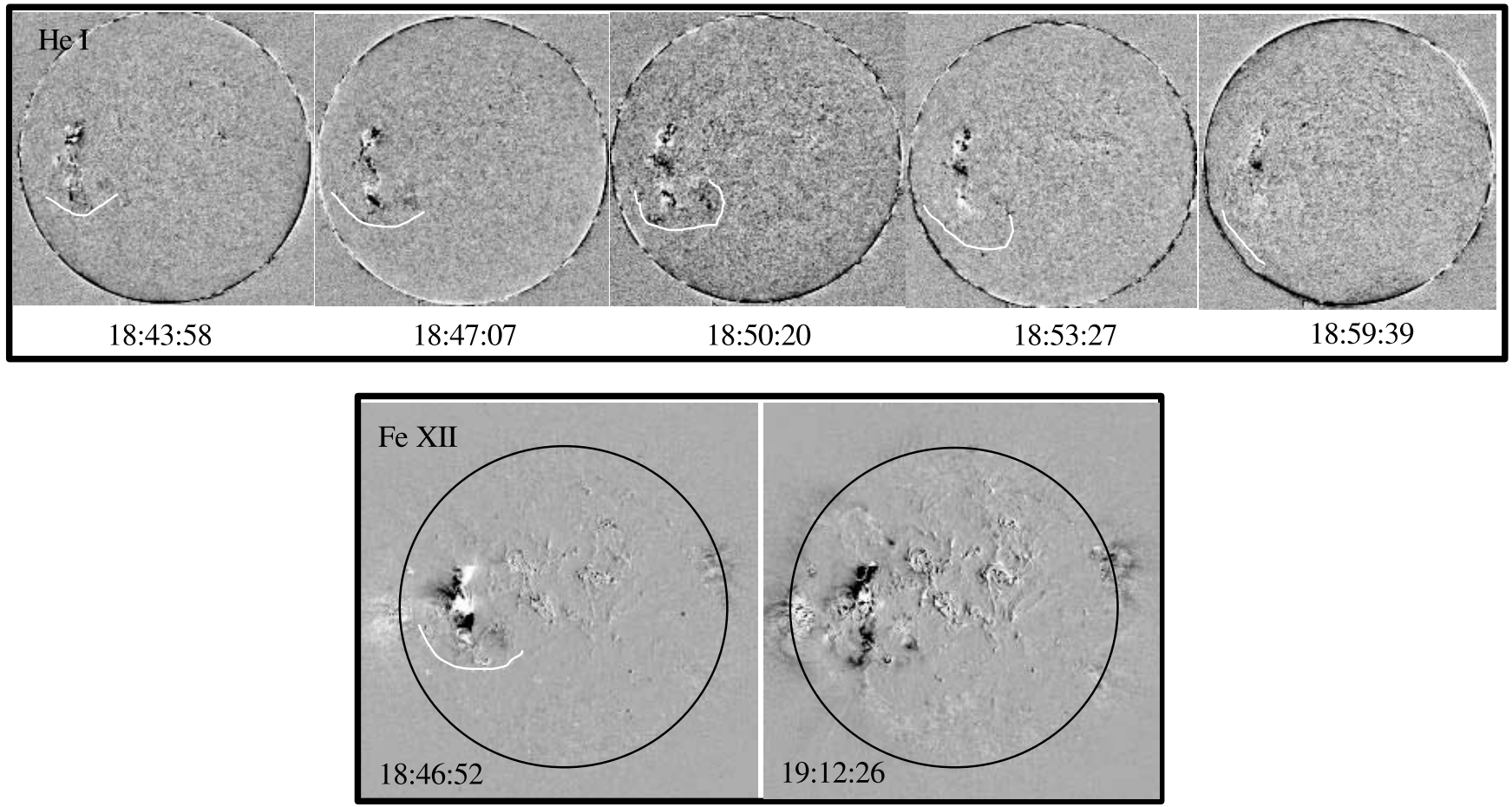

FIG. 2.—Running difference images showing the evolution of the wave event on 2001 January 20. The top panel shows the wave in five He I frames in which a line tracing out the front is added to aid in visualizing the wave evolution. The line is drawn by connecting a sequence of measurement points. The bottom panel shows the wave evolution in two EIT Fe XII images in which it is traced by a line in the first image (it is too diffuse in the second image to trace).

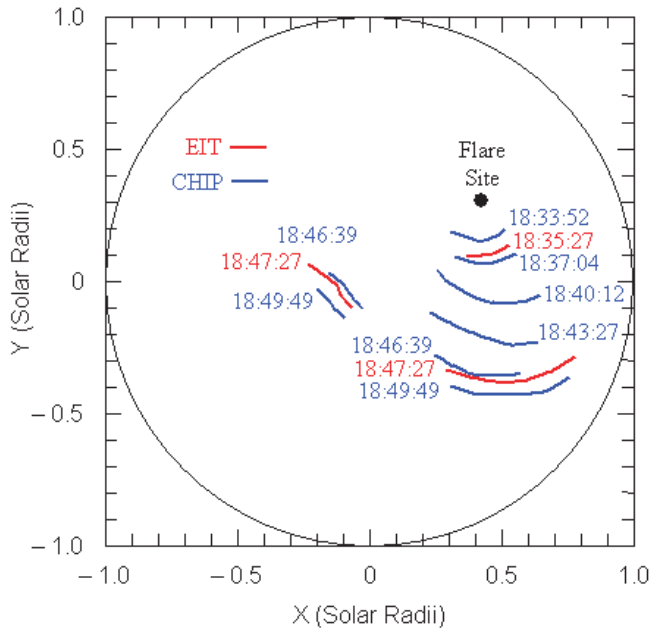

FIG. 3.—2000 November 25 wave front tracings (at all times measured) in both the Fe XII and He I data overlaid on a single grid in disk-center coordinates for an easier comparison of the spatial position in the two data sets. A small circle represents the flare site.

the column labeled $\delta s_{\rm fs}$), which arises from spreading of radiation from the coronal wave front as it travels downward to the chromosphere. Finally, we must correct for wave front motion occurring during the finite recombination time of singly ionized chromospheric helium (see § 4.2, the Appendix, and the column labeled $\delta s_{\rm rec}$ in the table). The final column in Table 1 lists the values of Δs, the corrected displacement of the CHIP and EIT fronts (i.e., the corrected value of Δs_0). Most of the corrected displacements for this day are less than the spatial resolution of the CHIP instrument, which is $0.0072R_0$, while the largest corrected displacement is only about twice the CHIP resolution (i.e., $\Delta s = 0.0152$ for scan 2 of the later observation period).

3.2. *2001 January 20*

Figure 2 shows the evolution of the wave observed on 2001 January 20 in differenced images (running) in the CHIP data (*top*) and EIT data (*bottom*). To determine the wave velocity and compare the position of the EIT wave with the CHIP wave, we overlay the measurements for the CHIP wave at times 18:43:58 and 18:47:07 UT with the measurements for the EIT wave at time 18:46:52 UT onto a grid in Figure 7. As was done for the first event, scans are produced perpendicular to the CHIP wave front to deduce velocities at different points on the traveling wave front (Fig. 8). Table 1 lists the results of the velocity measurements for 10 different scans performed on the CHIP wave. For this event, the velocity of the wave front ranges from 219 km s^{-1} at the eastern most part of the measured wave to 429 km s^{-1} at the western edge of the measured wave. The scans are also used to compare the position of the CHIP wave at time 18:47:07 UT with that of the EIT wave at time 18:46:52 UT, the results of which can be found at the bottom of Table 1. The comparison shows that the largest corrected displacement is $\Delta s = -0.0166R_0$, which is comparable to the largest corrected displacement for the November 25 wave. If we calculate the mean and standard deviation for all the measured corrected displacements on both days, we find $\Delta s = -0.0024 \pm 0.0018$. This mean displacement is only one third of the CHIP spatial resolution ($0.0072R_0$), and we conclude that within the uncertainties of our observations, the CHIP and EIT waves are cospatial.

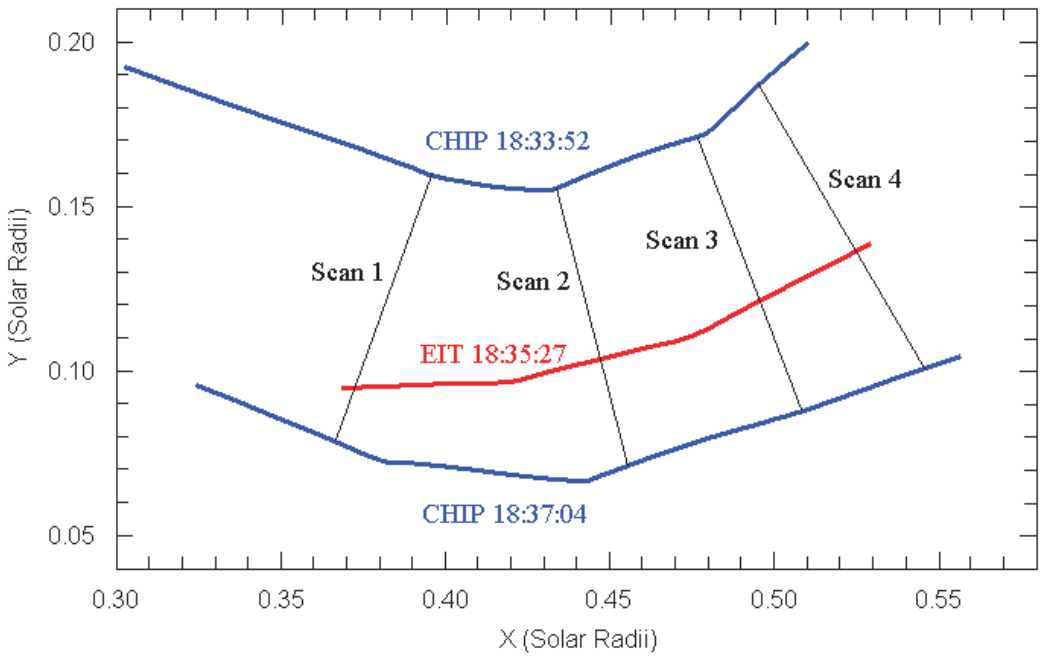

FIG. 4.—Close-up of the traced wave fronts on the grid in the region near the flare site for the 2000 November 25 event. The intensity fronts represented in this region correspond to CHIP times 18:33:52 and 18:37:04 UT and EIT time 18:35:27 UT. Scans are drawn perpendicular to the direction of propagation between the two CHIP waves to attain velocities at these different points in the CHIP wave evolution and to compare the spatial relationship between the CHIP wave and the EIT wave at these points in the different scans.

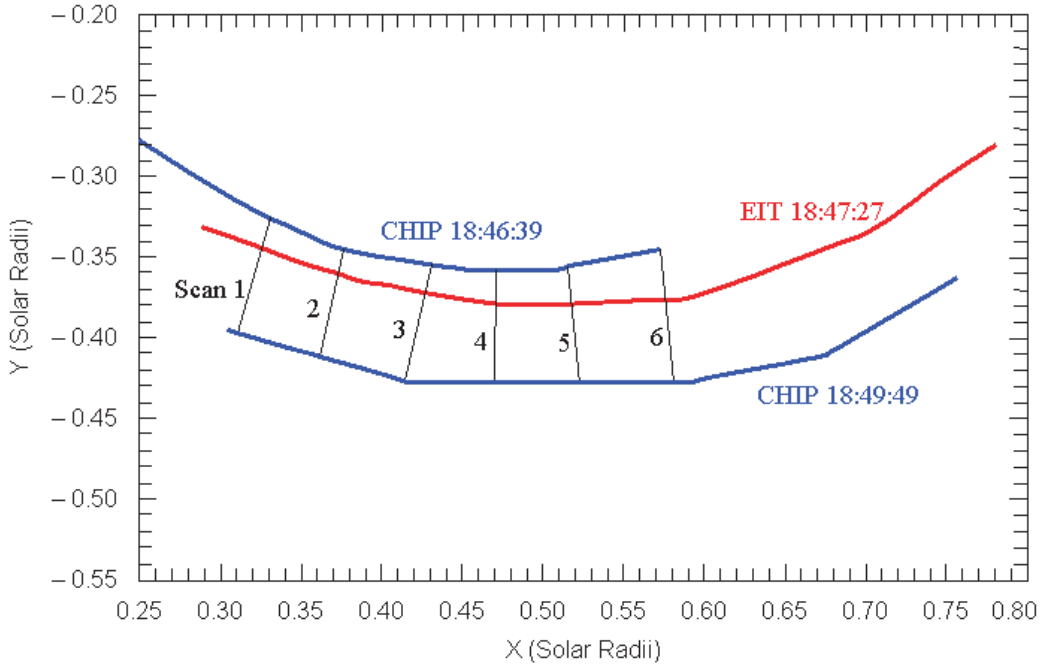

FIG. 5.—Close-up of the traced wave fronts on the grid in the region where the wave is traveling southward from the flare site for the 2000 November 25 event. The intensity fronts represented in this region correspond to CHIP times 18:46:39 and 18:49:49 UT and EIT time 18:47:27 UT. Scans are drawn perpendicular to the direction of propagation between the two CHIP waves to attain velocities at these different points in the CHIP wave evolution and to compare the spatial relationship between the CHIP wave and the EIT wave at these points in the different scans.

4. INTERPRETATION

4.1. *Formation of* He I λ10830

After determining (with some degree of certainty) that these two chromospheric waves are cospatial with their coronal counterparts, we turn now to the interpretation of that cospatiality. We believe that chromospheric waves observed in He I data are manifestations of the nature of the formation of the He I absorption line, so let us begin our interpretation by describing the physics underlying He I line formation.

We assume that in the regions where we observe the wave, the He I absorption line at 10830 Å is formed almost entirely in the upper chromosphere to a depth where coronal radiation capable of ionizing helium ($\lambda < 504$ Å) is able to penetrate

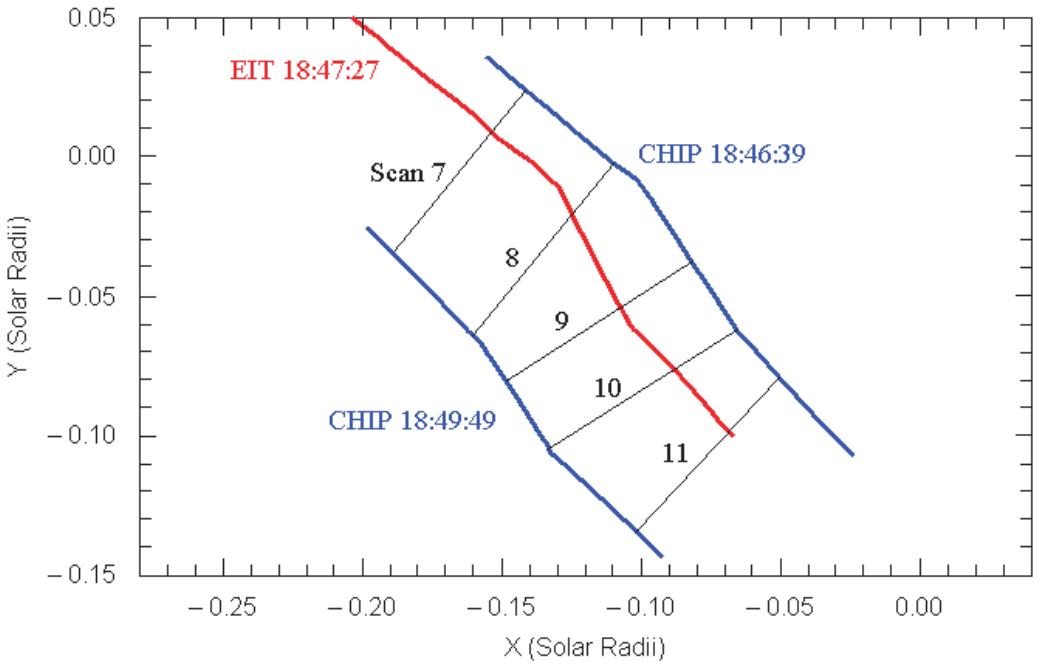

FIG. 6.—Close-up of the traced wave fronts on the grid in the region where the wave is traveling toward the southeast from the flare site for the 2000 November 25 event. The intensity fronts represented in this region correspond to the same CHIP times as Fig. 5: 18:46:39 and 18:49:49 UT and EIT time 18:47:27 UT. Scans are drawn perpendicular to the direction of propagation between the two CHIP waves to attain velocities at these different points in the CHIP wave evolution and to compare the spatial relationship between the CHIP wave and the EIT wave at these points in the different scans.

TABLE 1
DATA

Scan	x ($R_\odot$)	y ($R_\odot$)	dx/dy	V_{pos} ($R_\odot$ s^{-1})	Foreshortening	V (km s^{-1})	Δs_0 ($R_\odot$)	Δt (s)	δs_t ($R_\odot$)	δs_{rec} ($R_\odot$)	δs_{fs} ($R_\odot$)	Δs ($R_\odot$)
2000 Nov 11 (EIT 18:35:27; CHIP 18:33:52 and 18:37:04)												
1	0.383	0.12	0.36	4.66E−04	1.034	3.36E+02	−6.60E−02	95	4.43E−02	2.80E−02	−1.45E−02	−8.27E−03
2	0.447	0.113	−0.26	4.39E−04	1.000	3.06E+02	−5.13E−02	95	4.17E−02	2.63E−02	−1.50E−02	1.75E−03
3	0.494	0.13	−0.38	4.49E−04	1.002	3.13E+02	−5.20E−02	95	4.27E−02	2.69E−02	−1.50E−02	2.62E−03
4	0.523	0.145	−0.59	5.07E−04	1.014	3.58E+02	−5.66E−02	95	4.82E−02	3.04E−02	−1.48E−02	7.19E−03
2000 Nov 11 (EIT 18:47:27; CHIP 18:46:39 and 18:49:49)												
1	0.32	−0.36	0.26	3.70E−04	1.046	2.69E+02	−1.82E−02	48	1.78E−02	2.22E−02	−1.43E−02	7.42E−03
2	0.36	−0.378	0.18	4.04E−04	1.063	2.99E+02	−1.43E−02	48	1.94E−02	2.42E−02	−1.41E−02	1.52E−02
3	0.422	−0.39	0.21	3.56E−04	1.063	2.63E+02	−1.69E−02	48	1.71E−02	2.14E−02	−1.41E−02	7.44E−03
4	0.47	−0.392	0	3.43E−04	1.116	2.66E+02	−2.08E−02	48	1.65E−02	2.06E−02	−1.34E−02	2.80E−03
5	0.52	−0.392	−0.08	3.50E−04	1.151	2.80E+02	−2.21E−02	48	1.68E−02	2.10E−02	−1.30E−02	2.67E−03
6	0.578	−0.387	−0.09	4.04E−04	1.171	3.29E+02	−2.86E−02	48	1.94E−02	2.42E−02	−1.28E−02	2.22E−03
7	−0.165	−0.004	0.776	3.84E−04	1.006	2.69E+02	−1.77E−02	48	1.84E−02	2.30E−02	−1.49E−02	8.86E−03
8	−0.135	−0.033	0.867	4.09E−04	1.007	2.87E+02	−2.31E−02	48	1.96E−02	2.45E−02	−1.49E−02	6.17E−03
9	−0.115	−0.058	1.51	4.13E−04	1.008	2.90E+02	−3.08E−02	48	1.98E−02	2.48E−02	−1.49E−02	−1.07E−03
10	−0.1	−0.083	1.6	4.21E−04	1.008	2.95E+02	−2.62E−02	48	2.02E−02	2.53E−02	−1.49E−02	4.39E−03
11	−0.075	−0.106	0.963	3.93E−04	1.008	2.76E+02	−2.54E−02	48	1.89E−02	2.36E−02	−1.49E−02	2.17E−03
2001 Jan 20 (EIT 18:46:52; CHIP 18:43:58 and 18:47:07)												
1	−0.804	−0.31	0.76	1.79E−04	1.757	2.19E+02	−8.06E−03	−15	−2.69E−03	1.07E−02	−8.54E−03	−8.54E−03
2	−0.76	−0.345	0.73	2.30E−04	1.656	2.65E+02	−1.19E−02	−15	−3.45E−03	1.38E−02	−9.06E−03	−1.06E−02
3	−0.718	−0.371	0.727	2.82E−04	1.582	3.11E+02	−1.61E−02	−15	−4.23E−03	1.69E−02	−9.48E−03	−1.29E−02
4	−0.678	−0.4	0.444	3.07E−04	1.442	3.08E+02	−1.03E−02	−15	−4.61E−03	1.84E−02	−1.04E−02	−6.89E−03
5	−0.627	−0.419	0.17	2.73E−04	1.274	2.42E+02	−1.71E−02	−15	−4.10E−03	1.64E−02	−1.18E−02	−1.66E−02
6	−0.571	−0.429	0.04	2.82E−04	1.190	2.34E+02	−1.45E−02	−15	−4.23E−03	1.69E−02	−1.26E−02	−1.44E−02
7	−0.512	−0.418	−0.23	4.01E−04	1.073	3.00E+02	−1.55E−02	−15	−6.02E−03	2.41E−02	−1.40E−02	−1.14E−02
8	−0.459	−0.402	−0.45	5.12E−04	1.025	3.65E+02	−2.03E−02	−15	−7.68E−03	3.07E−02	−1.46E−02	−1.19E−02
9	−0.4	−0.376	−0.55	5.97E−04	1.013	4.21E+02	−2.32E−02	−15	−8.96E−03	3.58E−02	−1.48E−02	−1.11E−02
10	−0.332	−0.332	−0.69	6.14E−04	1.005	4.29E+02	−2.90E−02	−15	−9.21E−03	3.68E−02	−1.49E−02	−1.63E−02
Mean												−2.37E−03
Standard Deviation												1.83E−03

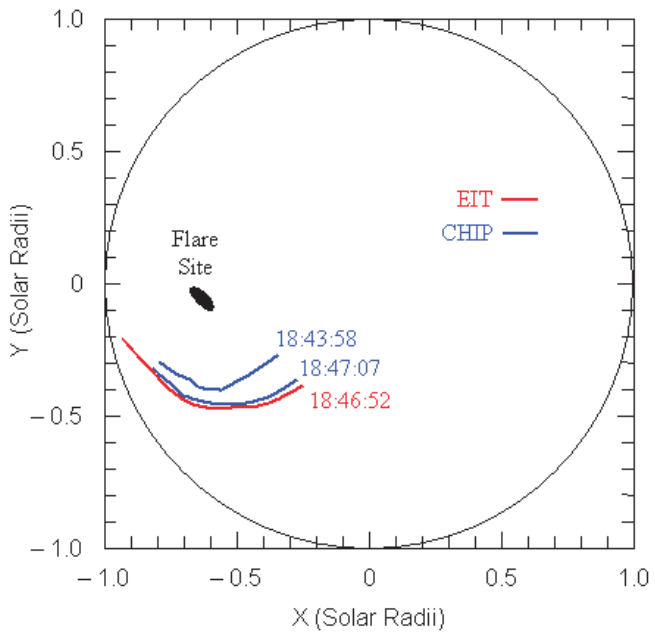

FIG. 7.—2001 January 20 wave front tracings (at all times measured) in both the Fe XII and He I data overlaid on a single grid in disk-center coordinates for an easier comparison of the spatial position in the two data sets. A small oval represents the flare site.

(e.g., Andretta & Jones 1997). It is, of course, possible that collisional excitation of the line in the lower transition region is significant, as assumed by Vršnak et al. (2002), but the fact that we see the wave clearly only in regions of relatively weak absorption has led us to use the results of Andretta & Jones (1997, Fig. 3) applicable to the quiet sun. The absorption of photospheric continuum radiation at 10830 Å depends on the (line-of-sight) column density of helium atoms in the $1s2s\ ^3S$ state, which absorb radiation at 10830 Å through a transition to the $1s2p\ ^3P^o$ state. Since the transition between the $1s2s\ ^3S$ state and the $1s^2\ ^1S$ state (i.e., the ground state of He I) is forbidden, the $1s2s\ ^3S$ state is populated through recombination of He II ions (since we are considering only chromospheric line formation and ignoring collisional excitation in the lower transition region). In the photoionization-recombination (PR) mechanism, the intensity of the He I 10830 Å absorption line should be approximately proportional to the intensity of the coronal radiation at wavelengths less than 504 Å penetrating the upper chromosphere.

4.2. *Possible Physical Explanation of the Observational Results*

The cospatiality of waves observed in He I with those observed in EIT leads us to conclude that chromospheric waves are not mechanical waves (viz., MHD waves) traveling horizontally through the upper chromosphere but are "imprints" (defined below) of the MHD waves traveling in the corona. If chromospheric waves were an extension of traveling coronal waves (both waves traveling outward from the flare), then they would lag behind the coronal waves, since the characteristic speed is much lower in the chromosphere. (Note that the temperature increases and the density decreases by some 2 orders of magnitude from the top of the chromosphere to the base of the corona, while the magnetic field intensity remains about the same; it follows that the fast-mode MHD speed is about an order of magnitude less at the top of the chromosphere than at the base of the corona.) We have shown that chromospheric waves do not lag behind the coronal waves but are cospatial. Our results are consistent with our assumptions concerning the formation of He I λ10830 (§ 4.1), because the bright front associated with the compressive wave traveling in the corona leads to an enhanced chromospheric absorption of the photospheric continuum at 10830 Å and thus a roughly cospatial dark front in the He I data. This is our definition of "imprint." The He I dark intensity wave front may not be

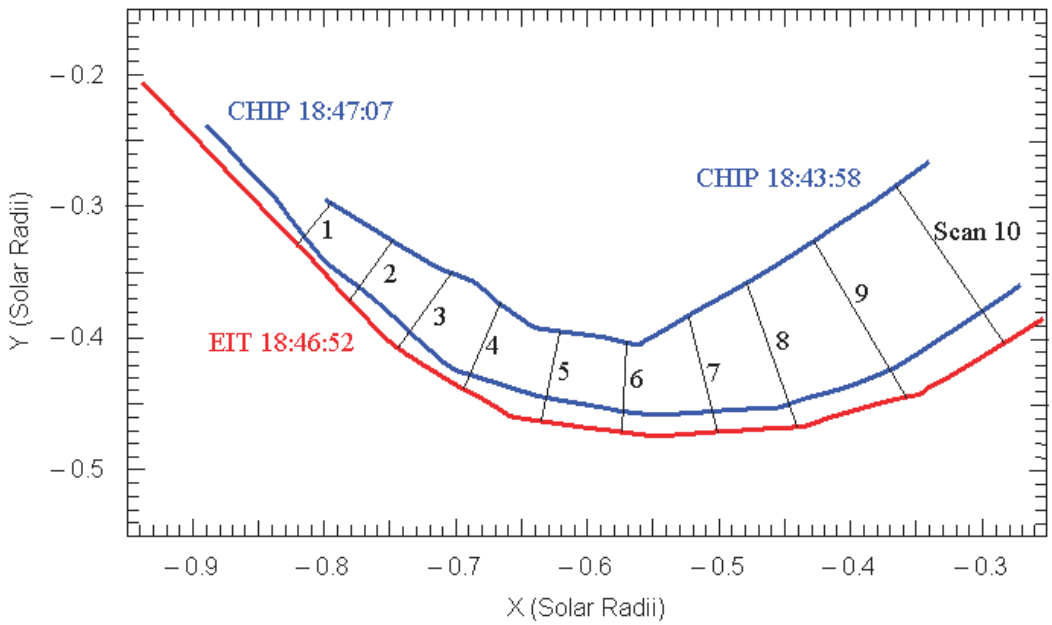

FIG. 8.—Close-up of the traced wave fronts on the grid in the region where the wave is traveling toward the southeast from the flare site for the 2001 January 20 event. The intensity fronts represented in this region correspond to CHIP times 18:43:58 and 18:47:07 UT and EIT time 18:46:52 UT. Scans are drawn perpendicular to the direction of propagation between the two CHIP waves to attain velocities at these different points in the CHIP wave evolution and to compare the spatial relationship between the CHIP wave and the EIT wave at these points in the different scans.

"exactly" cospatial with the coronal wave because a recombination time of 1 minute (see Appendix) is involved in the PR process of forming the He I absorption line. Because of this recombination time, the He I imprint of the coronal wave will tend to lag the coronal wave by a small distance, but there is another effect, which to some extent counters this small lag, and that is the spreading of the downward incident coronal radiation onto the chromosphere (see Appendix for details regarding both of these effects).

An alternative interpretation of He I λ10830 waves is presented in Vršnak et al. (2002) in which He I waves are analyzed and compared with waves observed in Hα. In their study, Vršnak et al. conclude the He I disturbances consist of two main parts: a forerunner (the shallow frontal segment) and a main dip, the latter being cospatial with the corresponding Hα disturbance. They interpret the cause of the main perturbation dip to be a sudden pressure jump in the corona that subsequently creates a fast-mode MHD shock front (the dip resulting when the shock front surpasses a given point in the chromosphere). The authors also suggest that the pressure jump behind the shock causes a density/temperature increase in the transition region (as well as in the chromosphere) so that the collisional processes are enhanced, leading to a population increase in the lowest level of the triplet state, and thus, an increase in He I absorption. In this picture, collisional processes are mainly responsible for increased He I absorption in the "main dip" of the wave, but increasing He I absorption via the PR mechanism (§ 4.1) is also discussed by Vršnak et al. They suggest the photoionization-recombination process may cause a He I enhancement in the diffuse component of the perturbation (they observe a diffuse component in the forerunner and the main dip). The existence of a nondiffuse component in the He I forerunner is explained as being a consequence of thermal conduction carrying energy along magnetic field lines into the upstream region of the shock (an oblique MHD shock exists in this picture). Our interpretation differs from that proposed by Vršnak et al. in two ways: (1) our waves have not necessarily steepened into shocks, and we do not have an inclined or curved front at low heights; and (2) the PR mechanism is the main cause of increased He I absorption in our interpretation, whereas it is only a secondary cause in their interpretation. Either way of interpreting He I waves may be valid, but it is difficult to distinguish between the two proposed pictures without performing complicated radiative transfer calculations, which is beyond the scope of this paper (see Andretta & Jones 1997).

One can conclude from the arguments presented above (either ours or those of Vršnak et al.) concerning He I absorption in chromospheric waves that "dimmings" observed in EIT as dark features (Thompson et al. 1998, 2000a; Zarro et al. 1999; Delannée, Delaboudinière, & Lamy 2000) should appear as cospatial "brightenings" in He I observations, and this is observed (G. de Toma 2004, private communication). Transient coronal holes, which produce dim regions in EUV observations, result from a decrease in density of the overlying corona (Zarro et al. 1999; Thompson et al. 2000a) caused by the opening of magnetic fields occurring during the expulsion of CMEs. Transient coronal hole evolution usually involves the expansion of dimming regions (Thompson et al. 1998), which may somewhat mimic the propagation of a wave, so careful attention needs to be paid to the observations in distinguishing between wave propagation and transient hole formation. In general, waves are observed propagating to much greater distances from their source region than the outward expansion of EIT dimmings or He I brightenings. EIT dimmings usually originate from the same general source region as the waves. Careful consideration was taken to distinguish between the transient coronal holes and the waves when we measured the two wave events in the present work.

5. CONCLUSIONS

Comparing waves observed in the chromosphere with those observed in the corona using He I λ10830 and Fe XII λ195 allows us to determine that the waves observed in the two lines are cospatial. This spatial relationship suggests that the chromospheric wave is not mechanical in nature (i.e., is not an MHD wave). We offer a physical explanation of these results based on the nature of the formation of the He I absorption line, concluding that the waves observed in the chromosphere are imprints of mechanical waves propagating through the corona. The same physical explanation can be used in trying to understand He I brightenings, which are associated with EIT dimmings.

Based on the physical explanation of our results, it is to be expected that any coronal compressive wave should have a detectable signature in He I λ10830, provided the coronal brightness enhancement associated with the wave front is sufficiently strong. For example, both the leading and trailing waves discussed by Uchida et al. (2001: see also Eto et al. 2002) would likely have such a detectable chromospheric He I signature. If their model is applicable to the waves studied here, then it is their trailing wave that we have considered in this paper. In any case, a high–time cadence He I λ10830 data set should provide an additional useful tool in the study of coronal waves.

APPENDIX

WAVE FRONT DISPLACEMENT AND SPREADING IN He I λ10830

Let us consider a coronal wave front that is bright in wavelengths ($<$504 Å) that can ionize He I from its ground state. We assume that the only effect this coronal wave front has on He I λ10830 absorption in the upper chromosphere is through photoionization (and subsequent recombination) of He I, which serves to populate the atomic levels that participate in the formation of He I λ10830 (viz., the $1s2s\ ^3S$ and $1s2p\ ^3P^o$ levels). We assume further that collisional population of these atomic states is unimportant (i.e., we ignore the lower transition region above $\sim$20,000 K). Even if the coronal wave front is an infinitesimally thick vertical plane, it will give rise to a chromospheric He I λ10830 absorption signature that is of finite horizontal thickness. The finite thickness of the chromospheric signature of the coronal wave front arises from two effects: (1) the coronal wave front illuminates the chromosphere not just directly beneath it, but also ahead of and behind it; (2) the finite recombination time for helium will modify the shape, the horizontal thickness, and the location of the chromospheric He I λ10830 absorption signature. We consider these two effects separately below.

A1. FINITE RECOMBINATION TIME

The absorption of photospheric continuum radiation at 10830 Å depends on the (line-of-sight) column density of helium atoms in the $1s2s\ ^3S$ state, which absorb radiation at 10830 Å through a transition to the $1s2p\ ^3P^o$ state. Since the transition between the $1s2s\ ^3S$ state and the $1s^2\ ^1S$ state (i.e., the ground state of He I) is forbidden, the $1s2s\ ^3S$ state is populated through recombination of He II ions (since we are ignoring collisional excitation that can be important at temperatures above ~20,000 K). In general, the local number density of atoms in the jth state (e.g., helium atoms in the $1s2s\ ^3S$ state) is determined by the jth species continuity equation:

$$\frac{\partial n_j}{\partial t} + \nabla \cdot n_j \boldsymbol{u}_j = q_j - l_j. \tag{A1}$$

In this equation q_j represents the production rate of the jth species in particles s^{-1}, while l_j represents the loss rate of the jth species in particles s^{-1}. For the present consideration, we will not take into account diffusion effects and thus will ignore the divergence term in equation (A1). This assumption means we will not have to consider the jth species momentum equation, nor will we consider the jth species energy equation, but instead we will assume that the temperature is given. Nevertheless the jth species continuity equation is generally coupled to one or more of the continuity equations for the other species under consideration (in this case, all the states of He I, He II, and He III). Rather than deal with such a highly coupled, complex system, we instead will consider only two continuity equations and deal with the ignored coupling qualitatively. These are the continuity equations for He I in the $1s2s\ ^3S$ state and for He II in its ground state, which are

$$\frac{\partial n}{\partial t} = \alpha n_{\rm II} n_e - \beta n, \tag{A2}$$

$$\frac{\partial n_{\rm II}}{\partial t} = \beta_{\rm I} n_{\rm I} - \alpha_{\rm I} n_{\rm II} n_e, \tag{A3}$$

where we have used no subscripts for quantities associated with the He I in the $1s2s\ ^3S$ state, a I subscript for He I in all states, a II subscript for He II in its ground state, and an e subscript for electrons. Here, α is the recombination coefficient into the $1s2s\ ^3S$ state, $\alpha_{\rm I}$ is the total recombination coefficient (into all He I states), β is the loss rate (dominated by ionization) for the $1s2s\ ^3S$ state, and $\beta_{\rm I}$ is the total ionization rate for He I. Because the ionization potential of the He I ground state is 24.6 eV (corresponding to a wavelength of 504 Å), $\beta_{\rm I}$ has a major component arising from photoionization by coronal radiation. In contrast, the ionization potential of the He I $1s2s\ ^3S$ state is only 4.8 eV (corresponding to a wavelength of 2600 Å), so β is not dominated by coronal radiation but rather by a combination of collisional ionization and photoionization by the photospheric continuum.

Now let us consider the characteristic timescales for the evolution of n and $n_{\rm II}$ in response to changes in production and loss rates. We define these two timescales as

$$\tau = \left| \frac{1}{n} \frac{\partial n}{\partial t} \right|^{-1} = \left| \frac{1}{\tau_r^{-1} - \tau_i^{-1}} \right|, \tag{A4}$$

$$\tau_{\rm II} = \left| \frac{1}{n_{\rm II}} \frac{\partial n_{\rm II}}{\partial t} \right|^{-1} = \left| \frac{1}{\tau_{{\rm II}r}^{-1} - \tau_{{\rm II}i}^{-1}} \right|, \tag{A5}$$

where we have defined the following ionization and recombination times (cf. eqs. [A2]–[A5]):

$$\tau_i = \beta^{-1}, \tag{A6}$$

$$\tau_r = \frac{n}{\alpha n_{\rm II} n_e}, \tag{A7}$$

$$\tau_{{\rm II}i} = \frac{n_{\rm II}}{\beta_{\rm I} n_{\rm I}}, \tag{A8}$$

$$\tau_{{\rm II}r} = \frac{1}{\alpha_{\rm I} n_e}. \tag{A9}$$

In equilibrium, the ionization and recombination timescales will be equal (i.e., the time derivative terms vanish in eqs. [A2] and [A3]). If we evaluate the equilibrium timescales at a height of 1990 km, the center of the region where we expect He I λ10830 to be formed for a temperature of 7000 K in the VAL-C model (Vernazza, Avrett, & Loeser 1981), we find

$$\tau_i = \tau_r \approx 10^{-3}\ {\rm s}, \tag{A10}$$

$$\tau_{{\rm II}i} = \tau_{{\rm II}r} \approx 60\ {\rm s}. \tag{A11}$$

Referring to equations (A4) and (A5), it is clear that these equilibrium timescales do not provide us directly with the relaxation timescales τ and $\tau_{\rm II}$, but they do provide a basis for further discussion. In the situation we are considering, we have an increase in $\beta_{\rm I}$

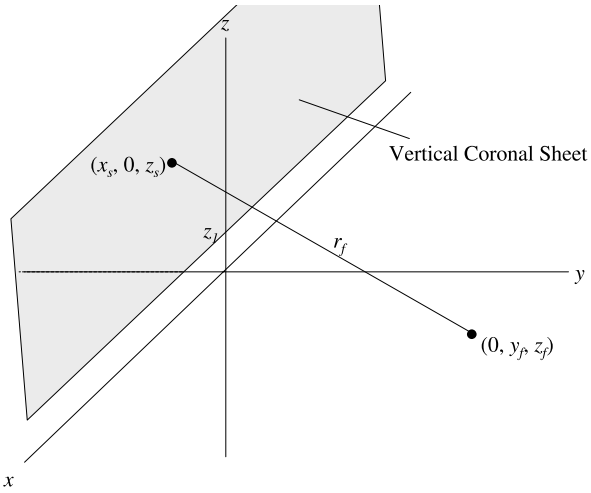

FIG. 9.—Schematic demonstrating an infinitesimally thin sheet of enhanced coronal radiation associated with a coronal wave front. The top of the chromosphere is located at $z = 0$, while the base of the corona (and thus the base of the coronal sheet) is located at $z = z_1$.

(owing to an increased photoionization by coronal radiation), driving n_{II} out of equilibrium and the consequent increase in n_{II} driving n out of equilibrium. If, for example, β_I increases by a factor of 2, which would eventually lead to a factor of 2 increase in n_{II}, the timescales given in equations (A10) and (A11) provide a good basis for estimating the relative relaxation times of n_{II} and n. In particular, we see that n relaxes so much faster than n_{II}, it is not unreasonable to treat the evolution of both as occurring on the timescale $\tau_{II} \approx \tau_{II} r$. In other words, the chromospheric signature (in He I λ10830 absorption) of enhanced coronal radiation will appear over a timescale τ_{II} from the time of the initial enhancement of the coronal illumination. We now turn to the subject of the illumination of the chromosphere by coronal radiation—specifically, the spreading of coronal radiation as it travels downward to the chromosphere.

A2. ILLUMINATION OF THE CHROMOSPHERE

Let us consider the radiation illuminating the chromosphere from a vertical coronal sheet in Figure 9. The vertical sheet shown in the figure can be thought of as an infinitesimally thin sheet of enhanced coronal radiation associated with a coronal wave front. In this coordinate system, the top of the chromosphere is located at $z = 0$, while the base of the corona (and thus the base of the coronal sheet) is located at $z = z_1$. A given point on the coronal sheet has the coordinates $(x_s, 0, z_s)$, while a point in the chromosphere whose illumination we will consider has the coordinates $(0, y_f, z_f)$. Note that we are considering chromospheric illumination only along a plane perpendicular to the center of the coronal sheet (i.e., in the $x = 0$ plane). If $\varphi(x_s, 0, z_s) dx_s\, dz_s$ represents the number of photons $\mathrm{sr}^{-1}\ \mathrm{s}^{-1}$ emanating from the differential area $dx_s\, dz_s$, then, in the absence of absorption, the photon flux density (photons $\mathrm{cm}^{-2}\ \mathrm{s}^{-1}$) at the point $(0, y_f, z_f)$ will be $[\varphi(x_s, 0, z_s)/r_f^2] dx_s dz_s$. The effect of chromospheric absorption will reduce this photon flux density by an exponential factor, so that we can represent the total photon flux density at $(0, y_f, z_f)$ from the entire coronal sheet by

$$I_f = \int\int \left[\varphi(x_s, 0, z_s)/r_f^2\right] e^{-\kappa}\, dx_s dz_s \text{ photons cm}^{-2}\ \text{s}^{-1}, \tag{A12}$$

where the integration is carried out over the entire sheet and

$$\kappa = \int_0^{r_f} (n_I \sigma_I + n_H \sigma_H)\, dr. \tag{A13}$$

Here the H subscript refers to neutral hydrogen, the I subscript is defined above, $r = 0$ at the point, $(x_s, 0, z_s)$, $r = r_f$ at the point $(0, y_f, z_f)$, and σ_j is the total cross section for absorption of coronal radiation by a j-type atom. Finally, if we assume that the ionization rate enhancement is directly proportional to the coronal photon flux density (i.e., $\Delta\beta_I \propto I_f$) and that an observer is looking vertically downward through the chromosphere, then the height-integrated ionization rate enhancement along the line of sight $(0, y_f)$ is

$$\Delta\beta_{If} \propto \int_{-\infty}^{0} I\, dz_f. \tag{A14}$$

In order to see how broad a region in the y-direction will exhibit a chromospheric He I λ10830 absorption signature of the coronal wave front, we must evaluate equations (A12)–(A14) for a range of values of y_f. For this purpose, we assume

$$\varphi(x_s, 0, z_s) = \varphi_1 e^{-(z_s - z_1)/h_s}, \tag{A15}$$

$$n_I,\ n_H \propto e^{-z/h_f} \text{ for } z \leqslant 0,$$

$$n_I,\ n_H = 0 \text{ for } z > 0.$$

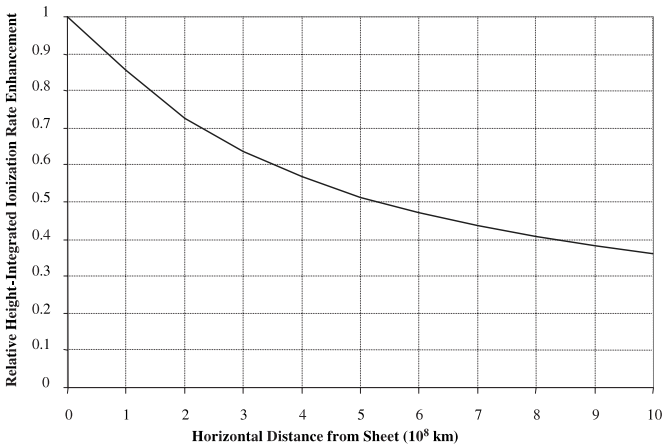

FIG. 10.—Variation with y of the height-integrated ionization enhancement for the representative case using the VAL-C model in which $z_1 = 600$ km (roughly the distance from the top of the chromosphere to the base of the corona in this model), and $h_f = 200$ km (approximately the density-squared scale height in the chromosphere).

In the above equations h_f and h_s represent the vertical scale height of density in the chromosphere and the vertical photon flux density scale height in the coronal sheet, respectively. Using the VAL-C model we choose a representative case in which $z_1 = 600$ km (roughly the distance from the top of the chromosphere to the base of the corona in this model), $h_f = 200$ km (approximately the density squared scale height in the chromosphere), $h_s = 40,000$ km (approximately the flux density squared scale height for a 10^6 K corona). If we take the width of the vertical coronal sheet to be $0.3R_0$ in the x-direction, we find through evaluation of equations (A12)–(A14) the variation with y of the height-integrated ionization enhancement shown in Figure 10. The maximum ionization rate enhancement occurs directly below the sheet, and the results in the figure are normalized to this maximum value. We note that the horizontal scale over which the ionization enhancement e-folds is about 10^4 km, which for a wave front speed of 350 km s^{-1} corresponds to a timescale of about 30 s. This timescale reflects the tendency of the radiation spreading out from the coronal wave front to produce a chromospheric signal on the order of 30 s prior to the passage of the coronal wave front. This tendency is, of course, countered by the delay associated with the He II recombination time of about 60 s given in equation (A11). Taken together, these effects would seem to imply a chromospheric He I λ10830 absorption front that lags the coronal wave front by less than 30 s.

REFERENCES

Andretta, V., & Jones, H. P. 1997, ApJ, 489, 375
Athay, R. G., & Moreton, G. E. 1961, ApJ, 133, 935
Biesecker, D. A., Myers, D. C., Thompson, B. J., Hammer, D. M., & Vourlidas, A. 2002, ApJ, 569, 1009
Cliver, E. W., Webb, D. F., & Howard, R. A. 1999, Sol. Phys., 187, 89
Delaboudinière, J. P., et al. 1995, Sol. Phys., 162, 291
Delannée, C., Delaboudinière, J. P., & Lamy, P. 2000, A&A, 355, 725
Elmore, D. F., et al. 1998, Appl. Opt., 37, 4270
Eto, S., et al. 2002, PASJ, 54, 481
Gilbert, H. R., & Holzer, T. E. 2004, ApJ, submitted
Khan, J. I., & Aurass, H. 2002, A&A, 383, 1018
Moreton, G. E. 1960, AJ, 65, 494
———. 1961, S&T, 21, 145
Neupert, W. M. 1989, ApJ, 344, 504
Pohjolainen, S., et al. 2001, ApJ, 556, 421
Smith, S. F., & Harvey, K. L. 1971, in Physics of the Solar Corona, ed. C. J. Macris (Dordrecht: Reidel), 156
Steinolfson, R. S., Wu, S. T., Dryer, M., & Tandberg-Hanssen, E. 1978, ApJ, 225, 259
Thompson, B. J., Cliver, E. W., Nitta, N., Delannee, C., & Delaboudiniere, J. 2000a, Geophys. Res. Lett., 27, 1431
Thompson, B. J., Plunkett, S. P., Gurman, J. B., Newmark, J. S., St. Cyr, O. C., & Michels, D. J. 1998, Geophys. Res. Lett., 25, 2465
Thompson, B. J., Reynolds, B., Aurass, H., Gopalswamy, N., Gurman, J. B., Hudson, H. S., Martin, S. F., & St. Cyr, O. C. 2000b, Sol. Phys., 193, 161
Thompson, B. J., et al. 1999, ApJ, 517, L151
Tousey, R. 1973, Space Res., 13, 713
Uchida, Y. 1968, Sol. Phys., 4, 30
Uchida, Y., Altschuler, M., & Newkirk, G., Jr. 1973, Sol. Phys., 28, 495
Uchida, Y., Tanaka, T., Hata, M., & Cameron, R. 2001, Publ. Astron. Soc. Australia, 18, 345
Vernazza, J. E., Avrett, E. H., & Loeser, R. 1981, ApJS, 45, 635 (VAL)
Vršnak, B., & Lulić, S. 2000, Sol. Phys., 196, 181
Vršnak, B., Warmuth, A., Brajša, R., & Hanslmeier, A. 2002, A&A, 394, 299
Warmuth, A., Vršnak, B., Aurass, H., & Hanslmeier, A. 2001, ApJ, 560, L105
Wills-Davey, M. J., & Thompson, B. J. 1999, Sol. Phys., 190, 467
Zarro, D. M., Sterling, A. C., Thompson, B. J., Hudson, H. S., & Nitta, N. 1999, ApJ, 520, L139